Atomic diffusion-induced polarization and superconductivity in topological insulator-based heterostructures

Xian-Kui Wei[1]*†, Abdur Rehman Jalil[2], Philipp Rüßmann[3,4]*, Yoichi Ando[5], Detlev Grützmacher[2], Stefan Blügel[4], Joachim Mayer[1,6]

[1]Ernst Ruska-Centre for Microscopy and Spectroscopy with Electrons, Forschungszentrum Jülich GmbH, 52425 Jülich, Germany

[2]Peter Grünberg Institute and JARA-FIT, Forschungszentrum Jülich GmbH, 52425 Jülich, Germany.

[3]Institute for Theoretical Physics and Astrophysics, University of Würzburg, 97074 Würzburg, Germany.

[4]Peter Grünberg Institute and Institute for Advanced Simulation, Forschungszentrum Jülich GmbH and JARA, 52425 Jülich, Germany.

[5]Physics Institute II, University of Cologne, Zülpicher Str. 77, 50937 Köln, Germany

[6]Central Facility for Electron Microscopy, RWTH Aachen University, Ahornstraße 55, 52074 Aachen, Germany.

*Corresponding author Emails: xkwei@xmu.edu.cn; p.ruessmann@fz-juelich.de

†Present address: College of Chemistry and Chemical Engineering, Xiamen University, 361005, Xiamen, China

ABSTRACT

The proximity effect at a highly transparent interface of an *s*-wave superconductor (S) and a topological insulator (TI) provides a promising platform to create Majorana zero modes in artificially designed heterostructures. However, structural and chemical issues pertinent to such interfaces are poorly explored so far. Here, we report the discovery of Pd diffusion induced polarization at interfaces between superconductive $Pd_{1+x}(Bi_{0.4}Te_{0.6})_2$ (xPBT, $0 \leq x \leq 1$) and Pd-intercalated Bi_2Te_3 by using atomic-resolution scanning transmission electron microscopy. Our quantitative image analysis reveals that nanoscale lattice strain and QL polarity synergistically suppress and promote the Pd diffusion at the normal and parallel interfaces, formed between Te-Pd-Bi triple layers (TLs) and Te-Bi-Te-Bi-Te quintuple layers (QLs), respectively. Further, our first-principles calculations unveil that the superconductivity of xPBT phase and topological nature of Pd-intercalated Bi_2Te_3 phase are robust against the broken inversion symmetry. These findings point out the necessity of considering coexistence of electric polarization with superconductivity and topology in such S-TI systems.

Keywords: topological insulator, superconductivity, polarization, atomic diffusion and intercalation, scanning transmission electron microscopy

INTRODUCTION

Majorana zero modes (MZMs) are one of the most exciting research topics in condensed matter systems owing to their potential applications in quantum computation.[1-3] In essence, MZMs obey non-Abelian braiding statistics.[4] Under unitary gate operation, the nonlocal encoding of the quasiparticle state makes the computation immune to certain type of error caused by local perturbation, thus leading to fault-tolerant computation.[5,6] Relying on non-trivial topological states of matter, the MZMs are predicted to emerge either in spinless p-wave topological superconductors (Ss) with one or two dimension,[7] or via proximity-induced superconductivity at interfaces of s-wave Ss with topological insulators (TIs).[8] Meanwhile, possible signatures of MZMs have also been unveiled in a number of systems like semiconductors,[9] quantum anomalous Hall insulators[10] and magnetic atomic chains[11] such as InSb-NbTiN,[12] Fe-Pb,[11] $FeTe_{0.55}Se_{0.45}$ superconductors,[13] EuS-Au[14] and LiFeAs.[15]

Given that topological Ss are scarce, implementing the interface-based proximity effect becomes a natural choice to pursue the MZMs and to construct heterostructure-based devices. Among various TIs such as HgTe, BiSb and $PbBi_2Te_4$,[16-18] 2D van der Waals (vdW) layered $(Bi_{1-x}Sb_x)_2Te_3$ has been widely investigated for its tunable topological surface state by chemical doping[19-21] and control of growth condition.[22,23] In spite of the ease in fabricating S-TI nanostructures, e.g., using stencil-lithography-based molecular-beam epitaxy,[24,25] such hybrid devices usually suffer issues about chemical diffusion, electronic structure change and interfacial dipole layers.[26,27] Therefore, clarifying the elemental diffusion mechanism and the fundamental physical properties at the interface becomes the urgent task towards creating stable MZMs in such hybrid S-TI devices.

Lately, $PdTe_2$-based Ss receive considerable attention owing to their intriguing band structure and transport property. Studies report that pure $PdTe_2$ is a Dirac semimetal with a superconducting T_C around 1.64 K.[28,29] By increasing the concentration of Pd, the T_C of $Pd_{1+x}Te_2$ ($x \geq 0$) can be increased to 4.5 K in metallic PdTe.[30,31] Although a potential phase boundary is expected in the structure-composition phase diagram,[31] a continuous $PdTe_2$-to-PdTe solid solution via gradual addition of Pd at the vdW gaps seems to refutes the existence of the boundary (Fig. 1A). Intriguingly, when metallic Pd is deposited on a TI like Bi_2Te_3 (Fig. 1B), a $PdTe_2$-like superconducting phase ($T_C \approx 0.6$ K) spontaneously forms at the interface through diffusing Pd into

the TI.[32] The newly formed fresh S/TI interface offers an alternative approach to create MZMs via the proximity effect.[33,34] Other than this, it has been claimed that Pd diffusion into Bi_2Te_3 can also lead to formation of a superconductive phase,[35,36] which indicates controversy about the origin of superconductivity.

In this work, in order to unravel the diffusion-based fundamental physics and device application, the diffusion pathway of Pd into the Bi_2Te_3 films grown on Si (111) substrates is investigated by using atomic-resolution scanning transmission electron microscopy (STEM) Unexpectedly, associated with observation of chemical intercalation, the Pd diffusion induced polarization is observed in the intermediate $Pd_{1+x}(Bi_{0.4}Te_{0.6})_2$ (xPBT, $0 \leq x \leq 1$) phase and at the xPBT/Bi_2Te_3 interfaces, i.e., at the normal vs parallel contact interfaces. Apart from disclosing the Pd diffusion pathway, our first-principles calculations reveal robustness of superconductivity for the xPBT and topology for the Pd-intercalated Bi_2Te_3 against the broken inversion symmetry. These findings highlight the necessity of exploring polarization-superconductivity-topology coupling in such S-TI systems.

RESULTS AND DISCUSSION

In our experiments, molecular beam epitaxy is used to grow the Bi_2Te_3 films (~18 nm) and a Pd layer (~6 nm) is deposited on top of Bi_2Te_3 to construct the S-TI heterostructures. Distinct from the Nb capped case,[24] our high-angle annular-dark field (HAADF) STEM imaging reveals that the capped Pd undergoes a spontaneous diffusion into the Bi_2Te_3, leading to formation of an intermediate $Pd_{1+x}(Bi_{0.4}Te_{0.6})_2$ (xPBT) phase between the Pd surface layer and the Bi_2Te_3 film (Fig. 1C). Although the Pd penetration depth varies according to the synthetic conditions, e.g., the substrate temperature during metal deposition,[33] thickness of the xPBT phase is observed to vary in the range of 6.8 to 8.6 nm in this specific case. As for roughness of the xPBT/Bi_2Te_3 interface, our energy dispersive X-ray spectroscopy (EDS) data reveals that this is attributed to quintuple layer (QL) terraces resulting from varied Pd diffusion depth into the TI (Fig. 1D).

The medium-resolution HAADF image shows that the xPBT phase is characteristic of a mixture of the $PdTe_2$- and PdTe-like triple layers (TLs), which consists of parallel and zigzag-type TLs due to inhomogeneous distribution of Pd atoms at the vdW gaps. In structure, the $PdTe_2$- and PdTe-like phases differ mainly in null and full occupancy of intercalated Pd atoms within the vdW

gaps[29] (Fig. 1A). This is substantiated by reproduction of the PdTe phase, previously determined to have $P6_3/mmc$ space group,[30] via adding one Pd atom at (0.0, 0.0, 0.5) site in the $PdTe_2$ (space group P-$3m$) framework (Supplementary Fig. S1). This also supports absence of the $PdTe_2$-PdTe phase boundary in the $Pd_{1+x}Te_2$ (0 ≤ x ≤ 1) phase diagram (Fig. 1A). One should note that the structure feature of the xPBT phase differs drastically from that of superconductive PdBiTe,[37] which has an intrinsic polar space group $P2_13$.

Further, we observe two kinds of interfaces near the QL terraces, a normal interface and a parallel one, which are defined in terms of crystal plane orientation (yellow and green dashed lines) in the TLs and QLs (Fig. 1E). In combination with geometric phase analysis (GPA),[38] we find that the a-axis difference between the xPBT and Bi_2Te_3 phases gives rise to an array of interfacial mismatch dislocations (average spacing ~7 nm), as manifested by in-plane ε_{xx} strain map (Fig. 1F). This is similar to mismatch dislocations observed at heterointerfaces of three-dimensional oxides.[39] Specifically, an out-of-plane ε_{zz} strain map differentiates the two contact interfaces. At the normal interface, the c-axis expansion is highly condensed at the first two TLs (width ~ 1.7 nm) with $\varepsilon_{zz\text{-}max} \approx 0.193$ (Fig. 1G,H). While at the parallel interface, the lattice expansion extends to about four TLs (width ~ 3.5 nm) with $\varepsilon_{zz\text{-}max} \approx 0.066$. By amplifying the ε_{zz} map, we see further details about z-direction lattice mismatch (Fig. 1I-K). Irrelevant to the interfacial contact manner, the local lattices (radius ~ 0.1 nm) on the left and right side of the dislocation cores are expanded and compressed, respectively. Our image analysis reveals that this arises from asymmetric agglomeration of Pd atoms near the dislocation cores (see Supplementary Fig. S2).
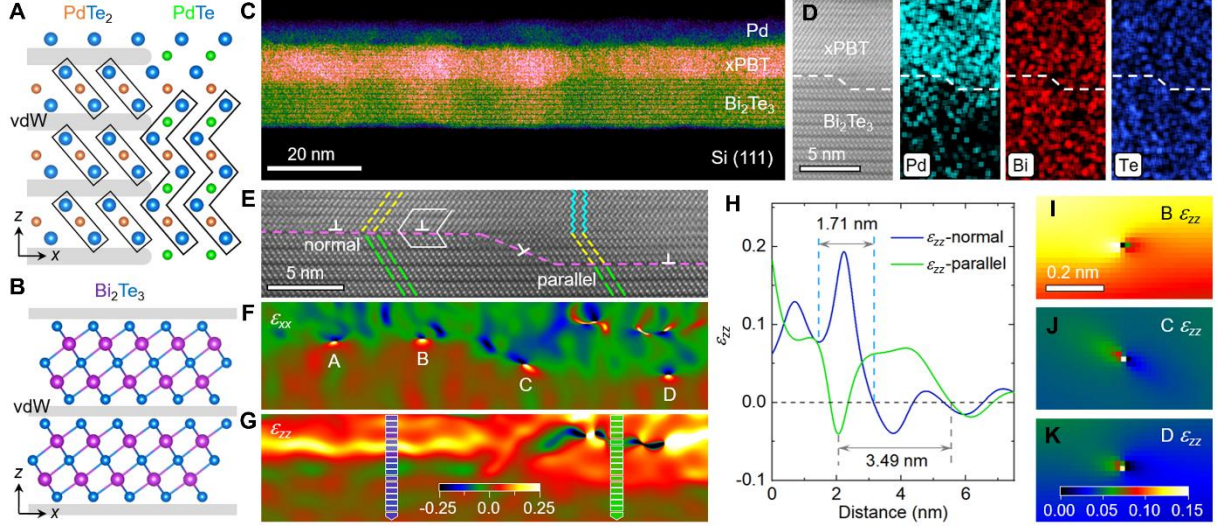
Figure 1. Intermediate xPBT phase and interfacial mismatch dislocations. (**A,B**) Crystal structures of PdTe$_2$, PdTe and Bi$_2$Te$_3$ viewed along [100] direction, respectively. The vdW gaps are denoted by grey stripes. (**C**) Low-magnification HAADF STEM image of a Pd/xPBT/Bi$_2$Te$_3$ heterostructure grown on Si (111) substrate. (**D**) HAADF image of a curved interface region and corresponding elemental EDX maps of Pd, Bi and Te. (**E-G**) Medium-magnification HAADF image of the interface and GPA strain maps of ε_{xx} and ε_{zz}, respectively. The burgers vector of the mismatch dislocations is $\vec{\mathbf{b}} = \mathbf{a}$ [100] on the flat (001) planes. The yellow, cyan, and green line segments denote the TLs and QLs, respectively. (**H**) Local strain line profile of ε_{zz} extracted from the normal and parallel interfaces illustrated in (**G**). (**I-K**) Magnified ε_{zz} strain maps near dislocations labeled by B, C and D in (**F**), respectively.

As for the Pd self-diffusion induced xPBT phase, the HAADF image contrast, proportional to $Z^{1.7}$ (Z, atomic number),[40] indicates that the intercalated Pd atoms at the vdW gaps exhibit an irregular occupancy between the TLs (Fig. 2A,C and Supplementary Fig. S3). This leads to nanoscale bending of the TLs (white dashed lines) and possible presence of flexoelectricity, i.e., coupling of strain gradient with polarization or vice versa. By measuring positions of atomic columns via 2D Gaussian functional fitting,[41] our mapping reveals a short-range Pd displacement order relative to centers of nearest-neighboring Bi/Te columns ($\delta_{Pd-Bi/Te}$) in the TLs (yellow arrows). On the other hand, the Pd atoms at vdW gaps between the TLs tend to exhibit an opposite displacement order (blue arrows). This gives rise to an oscillating polar feature as manifested by line profiles of $\delta z_{Pd-Bi/Te}$ and $\delta x_{Pd-Bi/Te}$, which are averaged along x direction (Fig. 2B). Specifically, the nanoscale ordering of Bi and Te atoms along z direction breaks the structural inversion

symmetry and thus leads to emergence of an intrinsic polar order. This is supported by non-negligible charge transfer from Bi/Te to Pd atoms owing to their difference in electronegativity, Bi ($\chi = 2.02$), Te (2.10) and Pd (2.20), as verified in nickel phosphides [42].

Near the xPBT/Bi_2Te_3 interface, the HAADF images show that a mixture of parallel and zigzag TLs dominate on the xPBT side, which is attributed to fractional occupancy of Pd at the vdW gaps (Fig. 2D,F). Nevertheless, more Pd atoms are observed to diffuse into the Bi_2Te_3 across the parallel interface, which is evidenced by more Pd atoms locating at the interstitial sites within the QLs (green circles). This reveals that the intermediate xPBT phase originates from dismembering the Bi-Te bonds of the QLs through the interstitial Pd atoms. On this basis, different dismemberment processes can be proposed to understand the Pd diffusion pathways at the two interfaces (see Supplementary Fig. S4). By measuring the interplanar spacing (d_{IPS}-c), we find that the a axis undergoes a sharp transition near the normal interface, while a gradual evolution is observed at the parallel interface (Fig. 2E,G). With respect to the average vdW spacing, $d_0 = 0.270 \pm 0.012$ nm, one can see that this value reduces to 0.228 nm and increases to 0.276 nm at the normal and parallel interface, respectively. This unveils that both in-plane and out-of-plane crystal spacings exhibit distinct responses to the suppressed and promoted Pd diffusion at the interfaces.
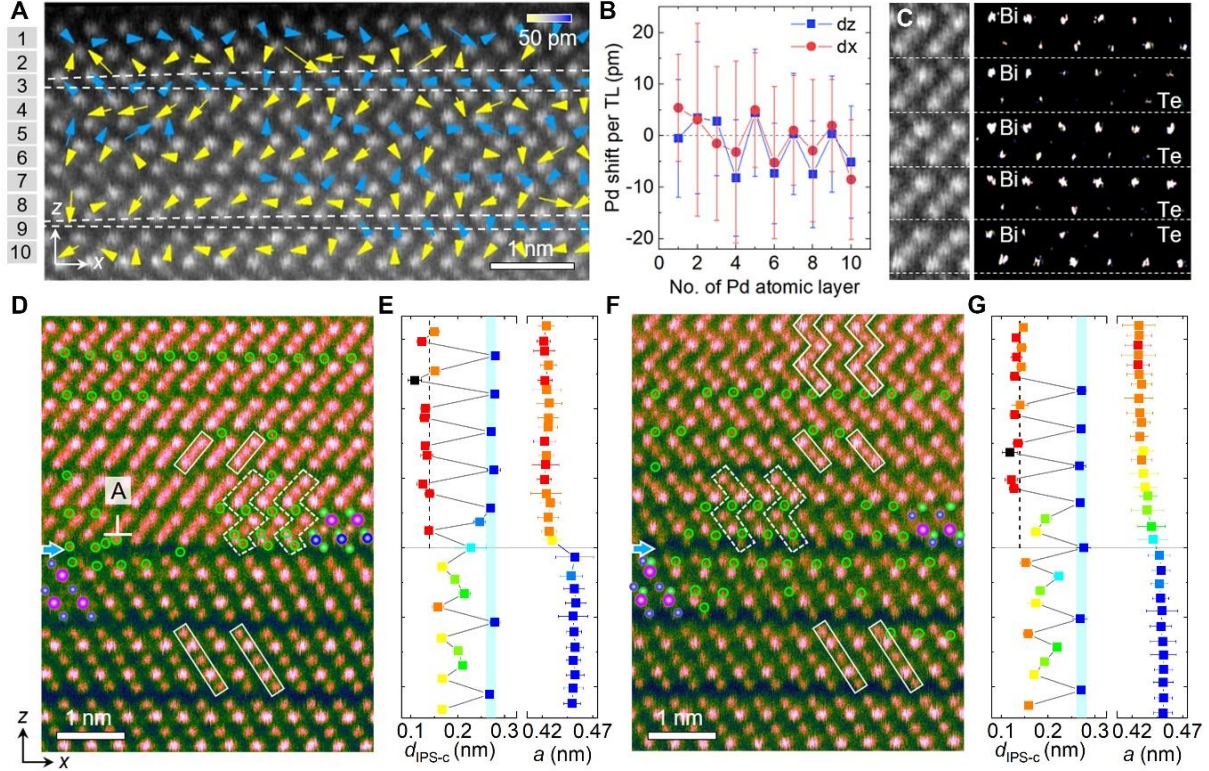
Figure 2. Pd diffusion induced polarity. (**A**) HAADF image of xPBT surface with overlapping of Pd displacements. (**B**) Averaged Pd displacements as a function of distance from the surface in the xPBT phase. (**C**) Intensity filtered HAADF image to illustrate the nanoscale ordering of Bi and Te arrangement. (**D,F**) Square-rooted atomic-resolution HAADF images of [100]-oriented xPBT/Bi_2Te_3 interfaces with normal and parallel contact, respectively. The discernable Pd columns are annotated by green circles. (**E,G**) Interplanar spacing (d_{IPS}) along z and a axis measured across the normal and parallel interfaces, respectively. The extreme values of the vdW spacing is determined by experimental (~0.261 nm) [43] and theoretical (~ 0.281 nm) data reported elsewhere [44,45].

In combination with image simulations with consideration of different Pd occupancy at the (0.0, 0.0, 0.5) site of the $Pd_x(Bi_{0.4}Te_{0.6})_2$ phase, our study reveals that the experimental specimen thickness is around 43.2 nm and the resolvable Pd concentration is ~0.35 (Supplementary Fig. S5). This implies that below this critical concentration, the intercalated Pd atoms within the vdW gaps and in the QLs of the Bi_2Te_3 cannot be directly identified. Associated with structural relaxation, our first-principles calculations further verify that the Pd diffusion at the interstitial positions of the Bi_2Te_3 is boosted by high-concentration intercalation of Pd atoms at the vdW gaps (Supplementary Figs. S6 and S7). Specifically, instead of the well-defined zigzag structures, the

parallel TLs linked by vdW gaps near the xPBT/Bi$_2$Te$_3$ interface play a crucial role in mediating the Pd diffusion across the interfaces, given that the vdW gaps offer large enough space for the dynamic migration of Pd atoms within the lattice matrix (Fig. 2D,F).

To deeply understand the effect of Pd diffusion, relative atomic displacements are mapped near the two xPBT/Bi$_2$Te$_3$ interfaces (Fig. 3A,D). On the xPBT side, by averaging the displacement values of $\delta_{\text{Pd-Bi/Te}}$ along x direction, one can see that the polarity frequently reverses its direction along z direction near the normal interface (Fig. 3B). This gives rise to positively charged head-to-head and negatively charged tail-to-tail vdW interfaces, as schematically illustrated in Fig. 3C. While near the parallel interface, the polarization gradient and head-to-head configuration result in positively charged wall interfaces (Fig. 3E,F). Since the Pd is more electronegative and thus more negatively charged than Bi and Te, this indicates that the parallel interface provides a more favorable condition for the diffusion of Pd into the Bi$_2$Te$_3$ than that at the normal interface. Correspondingly, we see that the in-plane polarity near the normal interface is larger than that near the parallel one, which should be a consequence of local lattice distortion caused by local Pd concentration (Fig. 1I-K).

On the Bi$_2$Te$_3$ side, we find that the Pd self-diffusion leads to development of net out-of-plane polarity in the first few QLs near the interface as well (see empty squares in Fig. 3B,D). This is referred to the primitive QLs, which are composed of octahedral BiTe$_6$ with antiparallel polarity and the total is null in polarity. Near the normal interface, the overall QL polarity points to the $-z$ direction. While near the parallel one, associated with a steady increase of the QL polarity as approaching the interface, the overall QL polarity points to the $+z$ direction. This reveals an interface-dependent switching behavior of polarization, which relates to different Pd diffusion pathways. By correlating with the observed Pd distribution, one can see that the $+z$-oriented QL polarity and head-to-head wall interfaces provide an attractive force for the diffusion of Pd atoms into the TI. Given the demand of polarization screening,[41,46] these results indicate that instead of electronic screening from the metallic xPBT, ionic migration via the Pd diffusion plays a major role in screening the QL polarity in the 2D layered TI. This interprets the suppression and promotion of Pd diffusion at the normal and parallel interface, respectively.
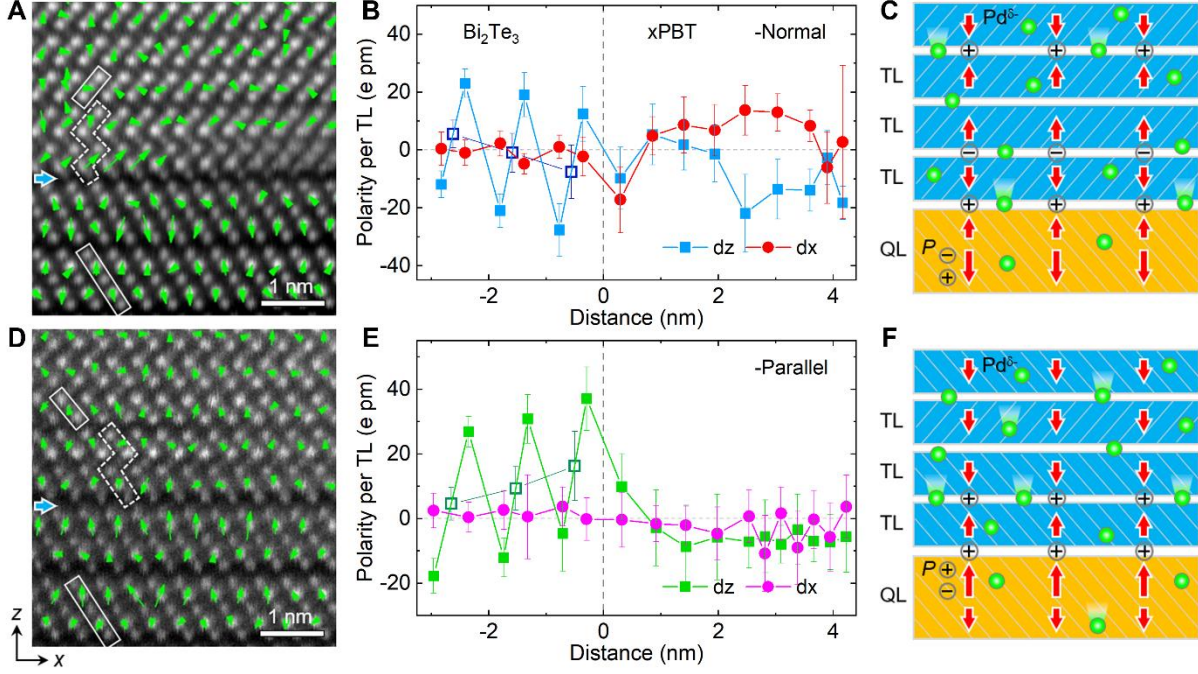
Figure 3. Polarity-mediated Pd diffusion near the interfaces. (**A,D**) Mapping of polar displacements of Pd and Bi against centers of their nearest-neighboring Te/Bi ($\delta_{Pd\text{-}Bi/Te}$) and Te columns ($\delta_{Bi\text{-}Te}$) near the normal and parallel xPBT/Bi$_2$Te$_3$ interface, respectively. (**B,E**) The polarity profiles (by taking the electron charge equals to one) per TL near the normal and the parallel interfaces, respectively. The empty squares denote the polarity per QL in the Bi$_2$Te$_3$. (**C,F**) Illustration of z-axis polarity mediated Pd diffusion near the head-to-head and tail-to-tail dipole interface, respectively. One should note that the electric dipole (pointing from negative to positive charges) direction in the xPBT phase (**A**) and (**D**) is reversed with respect to the polar displacement shown in (**B**) and (**E**), given the larger electronegativity of Pd (denoted by green circles, $\chi_{Pd} = 2.20$) than that of Te ($\chi_{Te} = 2.10$) and Bi ($\chi_{Bi} = 2.02$).

To establish a detailed structure-superconductivity relationship, we perform first-principles calculations using the KKR method[47] on four structural models of the xPBT phases, i.e., pure PdTe and PdTe$_2$ phases, a disordered alloy phase of Pd(Bi$_{0.4}$Te$_{0.6}$)$_x$ and an ordered alloy phase of Pd(BiTe)$_x$ with x = 1 or 2 (Fig. 4A-D). According to the BCS theory, the density of state around the Fermi energy, DOS(E_F), exponentially influences the superconducting gap and transition temperature. Compared with the normal-state electronic structures, which exhibit large changes between the PdTe and PdTe$_2$ phases, we find that the DOS(E_F) is reduced by about 25-30% as the

PdTe and PdTe$_2$ phases are disordered by random Bi substitution at their Te sites (Fig. 4E,F). Corresponding to an upward shift of the DOS curve, the overall downward shift of E_F thus indicates that the T_C of the xPBT phase is lowered with respect to the PdTe phase.

By taking the similar electron-phonon coupling coefficient (λ) in PdTe and PdTe$_2$, with λ = 0.58 and 0.65,[29,48] our modelling on the intrinsic s-wave pairing shows that the superconductivity of the xPBT phase is dominated by electronic degree of freedom and the change in metallicity (Fig. 4G and Supplementary Fig. S8). A detailed analysis on atom- and orbital-resolved contributions indicates that the Pd d-electrons are vital to stabilize the superconductivity (Supplementary Fig. S9). On the one hand, with respect to the PdTe$_x$ (x = 1 or 2) phases (see Table S1),[49-52] with a ratio of T_C[PdTe$_2$]/T_C[PdTe] = 1.7/4.5 = 0.38, its excellent agreement with our calculated ratio about superconducting order parameter χ, χ[PdTe$_2$]/χ[PdTe] = 0.37, unveils that an increasing Bi content tends to reduce the magnitude of χ and thus the T_C (Fig. 4H and Supplementary Fig. S10). One point worth noting is that an ordered Bi-Te arrangement in Pd$_2$BiTe (χ = 0.595), introducing an intrinsic polar order in the structure, increases the superconductive T_C with respect to the disordered Pd(Bi$_{0.4}$Te$_{0.6}$) phase (χ = 0.575), which has less Bi content compared with the Pd(Bi$_{0.5}$Te$_{0.5}$). On the other hand, analogous to the T_C difference between PdTe and PdTe$_2$, a decreasing Pd content also reduces the superconductive T_C as evidenced in the Pd$_2$BiTe and PdBiTe phases. Given that the short-range polar order can be averaged out on the length of tens of nanometers to several micrometers of the superconductive coherence length, we thus speculate that the larger experimental T_C (compared to pure PdTe$_2$) is attributed to mixing of the PdTe- and PdTe$_2$-like phases in xPBT, which results in an effectively larger average superconducting gap.
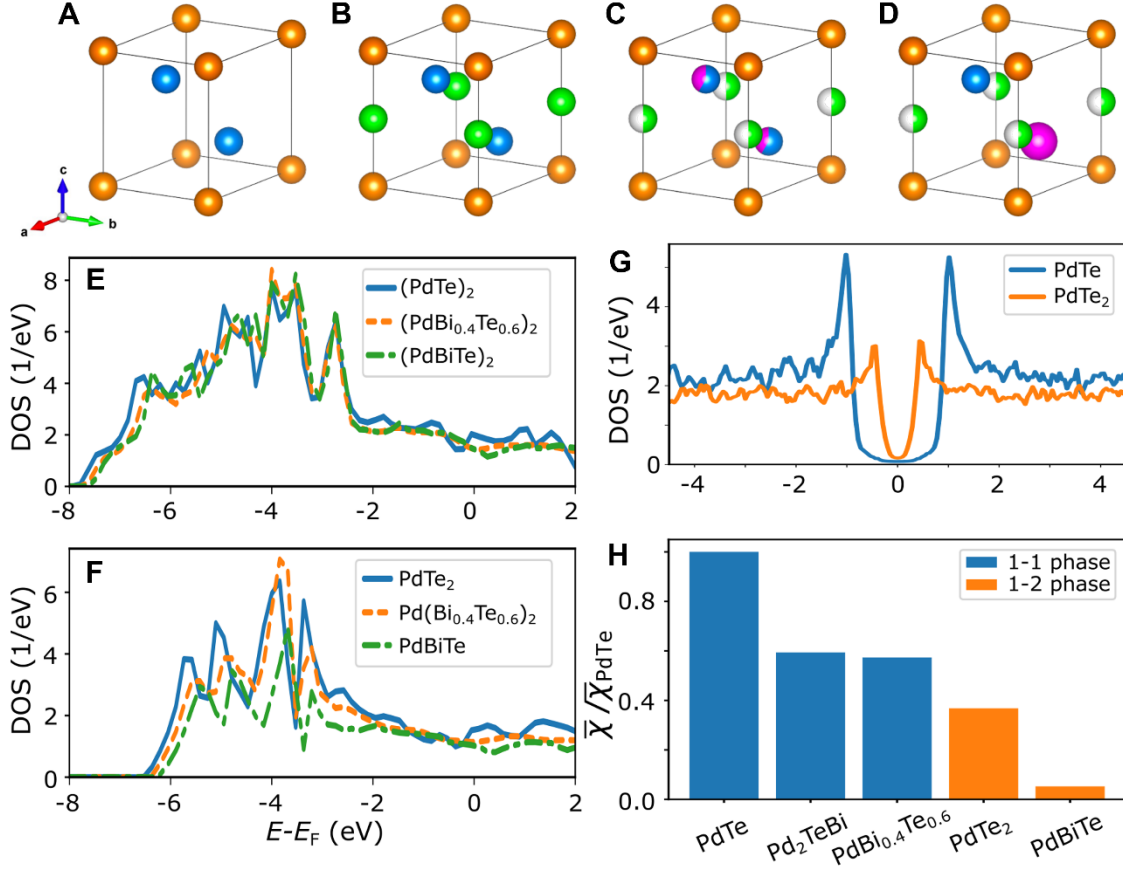
Figure 4. Electronic structure and superconductivity of the xPBT phase. (**A-D**) Crystal structure motifs of (**A**) $PdTe_2$, (**B**) PdTe, (**C**) random alloy $Pd_x(Bi_{0.4}Te_{0.6})_2$, (**D**) ordered alloy $Pd_{1+x}(BiTe)_2$ chosen for the DFT calculations. The spheres are color-coded as follows: Pd-orange, Te-blue, Bi-pink, intercalated Pd-green, where half-filled green spheres refer to either presence or absence of Pd in the $PdTe_x$ motif. (**E,F**) Normal state DOS of $(PdBi_{0.4}Te_{0.6})_2$ and $Pd(Bi_{0.4}Te_{0.6})_2$, respectively. (**G**) Superconducting gap in the DOS of PdTe and $PdTe_2$. (**H**) Magnitude of the average superconducting order parameter of different xPBT phases.

On this basis, we further calculate the band structures of relaxed $3 \times 3 \times 1$ Bi_2Te_3 supercells with different concentrations of Pd intercalated into the vdW gaps of the TI (Fig. 5A,D and Supplementary Fig. S6). Being consistent with our experimental observation, we find that the high Pd content intercalation mainly leads to structural relaxation along the z direction, where the underlying Bi atoms are pushed away from their high symmetry positions and unequal electric dipoles may form within the QL (Supplementary Fig. S7). Further, we investigate the robustness of the topological band inversion of the TI upon increasing Pd concentration. It is found that the

Pd d-bands form in the bulk bandgap region of Bi_2Te_3 (Fig. 5B,C and Supplementary Fig. S11). When Pd atoms diffuse into the QL structure at larger Pd concentration, the Pd d-bands move closer to the top of the valence band and a clear bandgap survives. This reveals that the intercalated Pd atoms and the induced polarity may largely modify the band structure of the Bi_2Te_3.

As is known, the topological phase transition in Bi_2Te_3 happens when the order of Bi p- and Te p-states become inverted around the Γ point due to the spin-orbit coupling (SOC).[53] Following the Te p-character of the bands around Γ upon activating SOC (Supplementary Fig. S12), our calculation proves that the topological phase transition stays intact at low Pd concentration. Although more Pd-derived impurity bands appear within the TI's bandgap, the topological band inversion is preserved even at larger concentration of Pd intercalation into the vdW gap of Bi_2Te_3 (Fig. 5E,F). One should note that the flat lines around E_F (highlighted by black arrows in Fig. 5) arise from d bands of the intercalated Pd atoms. Although the bands tend to hide the TI's bandgap, they do not break its topological nature. This is inferred from the surviving band inversion visible in the Te p-character upon including SOC (black ellipses in Fig. 5B,E). These results of the bulk electronic structure of Pd-intercalated Bi_2Te_3 suggest the robustness of topological surface states at the xPBT/Bi_2Te_3 interface. Therefore, a topological superconductor can be expected at such a S/TI heterostructure due to the good proximity effect.[4]
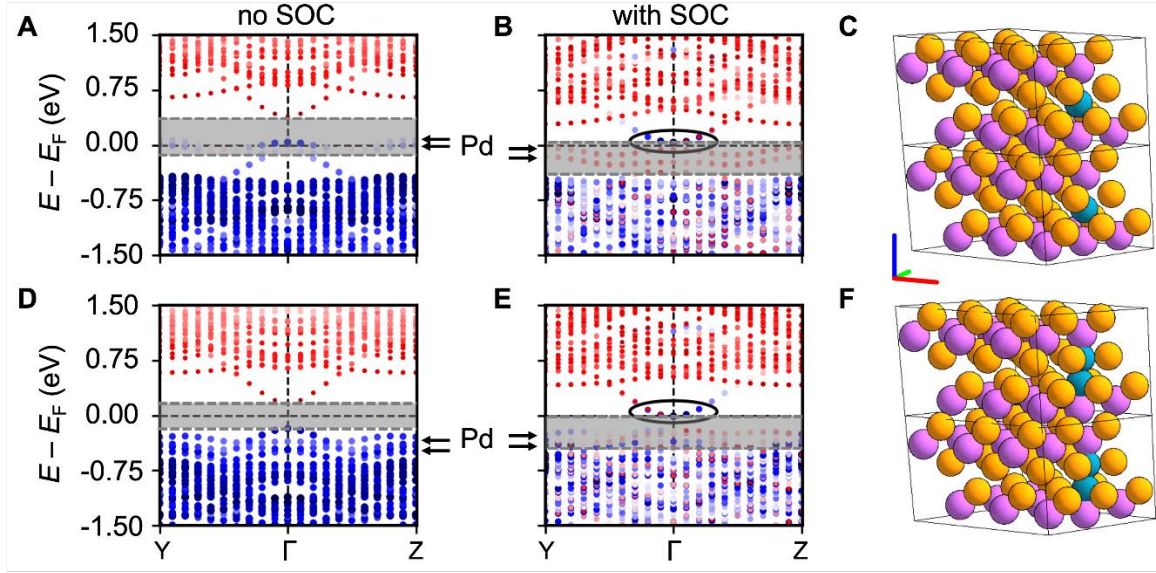
Figure 5. Band inversion in Bi₂Te₃ upon Pd diffusion. (A,B) Band structures calculated without and with consideration of the SOC for a $3 \times 3 \times 1$ supercell of Bi_2Te_3 (Bi-purple, Te-orange) with a single Pd atom intercalated into the vdW gap shown in (**C**). (**D,E**) Band structures without and with SOC for 2 Pd atoms intercalated into the vdW gap shown in (**F**). The red-white-blue coloring of the bands reflects that the TI conduction band is mainly composed of Te-p orbital character. The black ellipses highlight the topological band inversion visible in the transferred orbital character from red to blue in the bottom of the conduction band. The grey shaded areas indicate the TI's bandgap and location of the flat Pd impurity bands is indicated by the black arrows.

One question worth noting is that if the Pd diffusion happening only at the xPBT/Bi₂Te₃ interface, will the resulting metallic Pd d-states in the bandgap region stand in the way of realizing a topological superconductor? As is known, the recipe for engineering a topological superconductor in such an S/TI heterostructure requires: (i) existence of a topological surface state that can be proximitized; (ii) no other states that are not proximitized and thus close the proximity-induced gap in the electronic structure of the TI. Here we argue that both conditions are met at the xPBT/Bi₂Te₃ interface. While there are Pd d-derived states in the bandgap of the TI upon Pd diffusion, these are metallic states that are expected to hybridize well with the electronic structure of PdTe$_x$ due to their compatible orbital character. Because the Pd d-states in the xPBT phase are decisive in achieving robust superconductivity, one can conjecture that the Pd-d impurity states

may give rise to a sizable proximity gap and will thus be gapped out. The robustness of the topological phase transition upon Pd diffusion furthermore suggests that the topological surface state will be present at the xPBT/Bi$_2$Te$_3$ interface and can be proximitized.

The potential overlap and hybridization with Pd-derived states inside the TI's bulk band gap may even be beneficial for the hybridization of the TI's surface state with the superconductor. This may lead to larger proximity gaps in the topological surface state than without intercalated Pd atoms. Since the observed dislocations are accompanied with accumulation of Pd atoms on the xPBT side, our calculation results (Fig. 4H) show that this should rather strengthen the superconductivity of xPBT in these regions. Furthermore, since the coherence length, ranging from tens of nanometers to a few micrometers for PdTe and PdTe$_2$,[30,50] is much longer than the dislocation-related structural and compositional fluctuation (less than ~10 nm), we argue that there will be an averaging out of the superconductive gap on the length scale of the coherence length. Ultimately this leads to a robust superconducting gap in xPBT that can proximitize the TI surface state for generating the topological superconductivity. In addition, no significant charge transfer between the xPBT and TI phases is observed in our calculated band structures (Supplementary Fig. S12). This indicates that detrimental band bending effects unveiled in our earlier work on Nb/Bi$_2$Te$_3$ interface[54] are absent, which makes this S-TI interface a good candidate to engineer a topological superconductor.

CONCLUSIONS

In summary, our atomic-scale electron microscopy study reveals two distinct interfaces, the normal and parallel ones between the xPBT and Bi$_2$Te$_3$ phases. On the basis of quantitative image analysis, we find that the inhomogeneous Pd diffusion induces polarization in the xPBT phase and the Pd-intercalated Bi$_2$Te$_3$ phase, respectively. Specifically, it is found that the Pd diffusion is synergistically controlled by interfacial lattice strain and QL polarity, which inherently couple with the diffusion concentration of Pd atoms near the interfaces. Our first-principles calculations point out that the superconductivity of the xPBT phase is robust against the inversion symmetry breaking and chemical disorder. Although the Pd diffusion breaks the structural symmetry of the Bi$_2$Te$_3$, the metallic Pd-derived states in the bulk bandgap does not destroy the topological band inversion. These findings not only unravel the diffusion pathway of metals into the 2D layered TIs, which may apply to Nb-, Cu- or Sr-doped Bi$_2$Se$_3$ with nematic

superconductivity,[57,58] but also highlight the necessity of exploring the potential role of electric polarization[59] on electron pairing as studying MZMs in such S-TI heterostructures.

MATERIALS AND METHODS

Thin film growth: The samples were grown as thin films via molecular-beam epitaxy (MBE). First, 10×10 mm^2 Si(111) samples were prepared by a standard set of wafer cleaning steps (RCA-HF) to remove organic contaminations and the native oxide. A consecutive HF dip passivates the Si surfaces with hydrogen for the transfer into the MBE chamber (base pressure 5×10^{-10} mbar). To desorb the hydrogen from the surface, the substrates were heated up to 700 °C for 10 min and finally cooled down to 275 °C. The tellurium shutter was opened several seconds in advance to terminate the silicon surface by Te, which saturates the dangling bonds. Following this, standard Bi and Te effusion cells with vacuum being at 2.2×10^{-8} mbar and 5.7×10^{-7} mbar were heated to $T_{Bi} = 460$ °C and $T_{Te} = 260$ °C, respectively, for growth of the Bi$_2$Te$_3$ films. After this, the sample was cooled down to -20 °C (in vacuum) and the Pd was deposited via the e-beam evaporation on top of the Bi$_2$Te$_3$.

Scanning transmission electron microscopy experiments: For TEM observations, cross-sectional lamella specimens with a dimension of around 4 μm × 10 μm were cut along Si $[1\bar{1}0]$ direction using focused ion beam (FIB, FEI Helios NanoLab 400S) system and NanoMill (Model 1040) was used to mill down and remove the surface contamination. An FEI Titan 80-200 ChemiSTEM microscope equipped with a HAADF detector and a Super-X energy-dispersive X-ray spectrometer was used to collect the STEM image and EDX results. With a semi-convergent angle at 24.7 mrad, the HAADF images were collected in an angle range of 70 ~ 200 mrad. The Dr. Probe software package was used for image simulation,[60] and CrystalMaker and VESTA software packages were used for drawing the crystal structures. The lattice parameters of the xPBT and Bi$_2$Te$_3$ phases are measured and calibrated by referring to that of the Si substrate. The result shows that the lattice parameters is $a = 0.425 \pm 0.002$ nm and $c = 0.538 \pm 0.010$ nm for the xPBT phase, and $a = 0.451 \pm 0.001$ nm and $c = 3.013 \pm 0.015$ nm for the Bi$_2$Te$_3$ phase, respectively.

First-principles calculations: In our all-electron density functional theory (DFT) calculations we use the full-potential relativistic Korringa-Kohn-Rostoker Green function method (KKR)[61] as implemented in the JuKKR code[62] as well as the full-potential linearized augmented planewave (FLAPW) code FLEUR.[47] The FLEUR code is used for structural relaxations and the KKR method allows to describe random chemical disorder efficiently via the coherent potential approximation (CPA). The JuKKR code also comes with an extension to the Kohn-Sham-Bogoliubov-de Gennes method, which allows to calculate superconducting properties.[54,63] The series of DFT calculations in this study are orchestrated with the help of the AiiDA-KKR[64,65] and AiiDA-FLEUR[66,67] plugins to the AiiDA infrastructure.[68] This has the advantage that the full data provenance (including all values of numerical cutoffs and input parameters to the calculation) is automatically stored in compliance to the FAIR principles of open research data.[69] The complete data set of this project is made publicly available in the materials cloud archive.[70,71]

Data and code availability: The source codes of the AiiDA-KKR plugin,[65] the AiiDA-FLEUR plugin,[67] the JuKKR code,[62] and the FLEUR code[47] are published as open source software under the MIT license at https://github.com/JuDFTteam/aiida-kkr, https://github.com/JuDFTteam/aiida-fleur, https://iffgit.fz-juelich.de/kkr/jukkr, and https://iffgit.fz-juelich.de/fleur/fleur, respectively. The AiiDA dataset containing the DFT calculations of this work are published in the materials cloud archive [71]. The experimental data is available upon reasonable request.

ACKNOWLEDGEMENT

Author contributions

X.-K.W. conceived the research idea, performed the STEM experiments and analyzed the data with help of J.M. A.R.J. initiated the research and grew the thin films under the supervision of D.G. P.R. performed the DFT simulations and analyzed the results. S.B., Y.A. and J.M. contributed helpful discussion and useful sample information. X.-K.W. and P.R. wrote and revised the manuscript with comments from all co-authors.

Notes

The authors declare that they have no competing interests.

REFERENCES

(1)   Kitaev, A. Y. Fault-tolerant quantum computation by anyons. *Ann. Phys.* **2003**, *303*, 2-30.
(2)   Sarma, S. D.; Freedman, M.; Nayak, C. Majorana zero modes and topological quantum computation. *Npj Quantum Inf.* **2015**, *1*, 15001.
(3)   Lian, B.; Sun, X. Q.; Vaezi, A.; Qi, X. L.; Zhang, S. C. Topological quantum computation based on chiral Majorana fermions. *Proc. Natl. Acad. Sci. U.S.A.* **2018**, *115*, 10938-10942.
(4)   Alicea, J. New directions in the pursuit of Majorana fermions in solid state systems. *Rep. Prog. Phys.* **2012**, *75*, 076501.
(5)   Alicea, J.; Oreg, Y.; Refael, G.; von Oppen, F.; Fisher, M. P. A. Non-Abelian statistics and topological quantum information processing in 1D wire networks. *Nat. Phys.* **2011**, *7*, 412-417.
(6)   Nayak, C.; Simon, S. H.; Stern, A.; Freedman, M.; Das Sarma, S. Non-Abelian anyons and topological quantum computation. *Rev. Mod. Phys.* **2008**, *80*, 1083-1159.
(7)   Read, N.; Green, D. Paired states of fermions in two dimensions with breaking of parity and time-reversal symmetries and the fractional quantum Hall effect *Phys. Rev. B* **2000**, *61*, 10267.
(8)   Fu, L.; Kane, C. L. Superconducting proximity effect and majorana fermions at the surface of a topological insulator. *Phys. Rev. Lett.* **2008**, *100*, 096407.
(9)   Lutchyn, R. M.; Sau, J. D.; Das Sarma, S. Majorana fermions and a topological phase transition in semiconductor-superconductor heterostructures. *Phys. Rev. Lett.* **2010**, *105*, 077001.
(10)   Qi, X.-L.; Hughes, T. L.; Zhang, S.-C. Chiral topological superconductor from the quantum Hall state. *Phys. Rev. B* **2010**, *82*, 184516.

(11)   Nadj-Perge, S.; Drozdov, I. K.; Li, J.; Chen, H.; Jeon, S.; Seo, J.; MacDonald, A. H.; Bernevig, B. A.; Yazdani, A. Observation of Majorana fermions in ferromagnetic atomic chains on a superconductor. *Science* **2014**, *346*, 602-607.

(12)   Mourik, V.; Zuo, K.; Frolov, S. M.; Plissard, S. R.; Bakkers, E. P. A. M.; Kouwenhoven, L. P. Signatures of majorana fermions in hybrid superconductor-semiconductor nanowire devices. *Science* **2012**, *336*, 1003-1007.

(13)   Wang, D.; Kong, L.; Fan, P.; Chen, H.; Zhu, S.; Liu, W.; Cao, L.; Sun, Y.; Du, S.; Schneeloch, J.; Zhong, R.; Gu, G.; Fu, L.; Ding, H.; Gao, H.-J. Evidence for Majorana bound statesin an iron-based superconductor. *Science* **2018**, *362*, 333-335.

(14)   Manna, S.; Wei, P.; Xie, Y.; Law, K. T.; Lee, P. A.; Moodera, J. S. Signature of a pair of Majorana zero modes in superconducting gold surface states. *Proc. Natl. Acad. Sci. U.S.A.* **2020**, *117*, 8775-8782.

(15)   Li, M.; Li, G.; Cao, L.; Zhou, X.; Wang, X.; Jin, C.; Chiu, C. K.; Pennycook, S. J.; Wang, Z.; Gao, H. J. Ordered and tunable Majorana-zero-mode lattice in naturally strained LiFeAs. *Nature* **2022**, *606*, 890-895.

(16)   Qi, X.-L.; Zhang, S.-C. Topological insulators and superconductors. *Rev. Mod. Phys.* **2011**, *83*, 1057-1110.

(17)   Kuroda, K.; Miyahara, H.; Ye, M.; Eremeev, S. V.; Koroteev, Y. M.; Krasovskii, E. E.; Chulkov, E. V.; Hiramoto, S.; Moriyoshi, C.; Kuroiwa, Y.; et al. Experimental verification of $PbBi_2Te_4$ as a 3D topological insulator. *Phys. Rev. Lett.* **2012**, *108*, 206803.

(18)   Zhang, X.; Liu, Q.; Xu, Q.; Dai, X.; Zunger, A. Topological insulators versus topological dirac semimetals in honeycomb compounds. *J. Am. Chem. Soc.* **2018**, *140*, 13687-13694.

(19)   Arakane, T.; Sato, T.; Souma, S.; Kosaka, K.; Nakayama, K.; Komatsu, M.; Takahashi, T.; Ren, Z.; Segawa, K.; Ando, Y. Tunable Dirac cone in the topological insulator $Bi_{2-x}Sb_xTe_{3-y}Se_y$. *Nat. Commun.* **2012**, *3*, 636.

(20)   Kong, D.; Chen, Y.; Cha, J. J.; Zhang, Q.; Analytis, J. G.; Lai, K.; Liu, Z.; Hong, S. S.; Koski, K. J.; Mo, S. K.; Hussain, Z.; Fisher, I. R.; Shen, Z. X.; Cui, Y. Ambipolar field effect in the ternary topological insulator $(Bi_xSb_{1-x})_2Te_3$ by composition tuning. *Nat. Nanotechnol.* **2011**, *6*, 705-709.

(21)   Chen, Y. L.; Analytis, J. G.; Chu, J.-H.; Liu, Z. K.; Mo, S.-K.; Qi, X. L.; Zhang, H. J.; Lu, D. H.; Dai, X.; Fang, Z.; Zhang, S. C.; Fisher, I. R.; Hussain, Z.; Shen, Z.-X. Experimental realization of a three-dimensional topological insulator, Bi_2Te_3. *Science* **2009**, *325*, 178-181.

(22)   Wang, G.; Zhu, X. G.; Sun, Y. Y.; Li, Y. Y.; Zhang, T.; Wen, J.; Chen, X.; He, K.; Wang, L. L.; Ma, X. C.; Jia, J. F.; Zhang, S. B.; Xue, Q. K. Topological insulator thin films of Bi_2Te_3 with controlled electronic structure. *Adv. Mater.* **2011**, *23*, 2929-2932.

(23)   Chuang, P.-Y.; Su, S.-H.; Chong, C.-W.; Chen, Y.-F.; Chou, Y.-H.; Huang, J.-C.-A.; Chen, W.-C.; Cheng, C.-M.; Tsuei, K.-D.; Wang, C.-H.; Yang, Y.-W.; Liao, Y.-F.; Weng, S.-C.; Lee, J.-F.; Lan, Y.-K.; Chang, S.-L.; Lee, C.-H.; Yang, C.-K.; Su, H.-L.; Wu, Y.-C. Anti-site defect effect on the electronic structure of a Bi_2Te_3 topological insulator. *RSC Adv.* **2018**, *8*, 423-428.

(24)   Schuffelgen, P.; Rosenbach, D.; Li, C.; Schmitt, T. W.; Schleenvoigt, M.; Jalil, A. R.;

Schmitt, S.; Kolzer, J.; Wang, M.; Bennemann, B.; et al. Selective area growth and stencil lithography for in situ fabricated quantum devices. *Nat. Nanotechnol.* **2019**, *14*, 825-831.

(25)   Breunig, O.; Ando, Y. Opportunities in topological insulator devices. *Nat. Rev. Phys.* **2021**, *4*, 184-193.

(26)   Noesges, B. A.; Zhu, T.; Repicky, J. J.; Yu, S.; Yang, F.; Gupta, J. A.; Kawakami, R. K.; Brillson, L. J. Chemical migration and dipole formation at van der Waals interfaces between magnetic transition metal chalcogenides and topological insulators. *Phys. Rev. Mater.* **2020**, *4*, 054001.

(27)   Walsh, L. A.; Smyth, C. M.; Barton, A. T.; Wang, Q.; Che, Z.; Yue, R.; Kim, J.; Kim, M. J.; Wallace, R. M.; Hinkle, C. L. Interface chemistry of contact metals and ferromagnets on the topological insulator Bi_2Se_3. *J.Phys. Chem. C* **2017**, *121*, 23551-23563.

(28)   Leng, H.; Orain, J. C.; Amato, A.; Huang, Y. K.; de Visser, A. Type-I superconductivity in the Dirac semimetal $PdTe_2$ probed by µSR. *Phys. Rev. B* **2019**, *100*, 23551-23563.

(29)   Anemone, G.; Casado Aguilar, P.; Garnica, M.; Calleja, F.; Al Taleb, A.; Kuo, C.-N.; Lue, C. S.; Politano, A.; Vázquez de Parga, A. L.; Benedek, G.; Farías, D.; Miranda, R. Electron–phonon coupling in superconducting 1T-$PdTe_2$. *Npj 2D Mater. Appl.* **2021**, *5*, 25.

(30)   Tiwari, B.; Goyal, R.; Jha, R.; Dixit, A.; Awana, V. P. S. PdTe: a 4.5 K type-II BCS superconductor. *Supercond. Sci. Technol.* **2015**, *28*, 055008.

(31)   Kjekshus, A.; Pearson, W. B. Constitution and magnetic and electrical properties of palladium tellurides ($PdTe-PdTe_2$). *Can. J. Phys.* **1965**, *43*, 438.

(32)   Bai, M.; Yang, F.; Luysberg, M.; Feng, J.; Bliesener, A.; Lippertz, G.; Taskin, A. A.; Mayer, J.; Ando, Y. Novel self-epitaxy for inducing superconductivity in the topological insulator $(Bi_{1-x}Sb_x)_2Te_3$. *Phys. Rev. Mater.* **2020**, *4*, 094801.

(33)   Bai, M.; Wei, X.-K.; Feng, J.; Luysberg, M.; Bliesener, A.; Lippertz, G.; Uday, A.; Taskin, A. A.; Mayer, J.; Ando, Y. Proximity-induced superconductivity in $(Bi_{1-x}Sb_x)_2Te_3$ topological-insulator nanowires. *Commun. Mater.* **2022**, *3*, 20.

(34)   Singh, Y. A. The H-T and P-T phase diagram of the superconducting phase in $Pd:Bi_2Te_3$. *J. Supercond. Nov. Magn.* **2016**, *29*, 1975-1979.

(35)   Sharma, M. M.; Sang, L.; Rani, P.; Wang, X. L.; Awana, V. P. S. Bulk superconductivity below 6 K in $PdBi_2Te_3$ topological single crystal. *Journal of Superconductivity and Novel Magnetism* **2020**, *33*, 1243-1247.

(36)   Hor, Y. S.; Checkelsky, J. G.; Qu, D.; Ong, N. P.; Cava, R. J. Superconductivity and non-metallicity induced by doping the topological insulators Bi_2Se_3 and Bi_2Te_3. *J. Phys. Chem. Solids* **2011**, *72*, 572-576.

(37)   Childs, J. D., Hall, S. R., The crystal structure of michenerite, PdBiTe. *Can. Mineral.* **1973**, *12*, 61-65.

(38)   M. J. Hytch, E. Snoeck, R. Kilaas, Quantitative measurement of displacement and strain fields from HREM micrographs. *Ultramicroscopy* **1998**, *74*, 131-146.

(39)   Wei, X.-K.; Vaideeswaran, K.; Sandu, C. S.; Jia, C.-L.; Setter, N. Preferential creation of polar translational boundaries by interface engineering in antiferroelectric $PbZrO_3$ thin films. *Adv. Mater. Interfaces* **2015**, *2*, 1500349.

(40)   Nellist, P. D.; Pennycook, S. J. The principles and interpretation of annular dark-field Z-contrast imaging. *Adv. Imaging Electron Phys.* **2000**, *113*, 147-203.

(41)   Wei, X.-K.; Yang, Y.; McGilly, L. J.; Feigl, L.; Dunin-Borkowski, R. E.; Jia, C.-L.; Bellaiche, L.; Setter, N. Flexible polarization rotation at the ferroelectric/metal interface as a seed for domain nucleation. *Phys. Rev. B* **2018**, *98*, 020102(R).

(42)   Wei, X. K.; Bihlmayer, G.; Zhou, X.; Feng, W.; Kolen'ko, Y. V.; Xiong, D.; Liu, L.; Blugel, S.; Dunin-Borkowski, R. E. Discovery of real-space topological ferroelectricity in metallic transition metal phosphides. *Adv. Mater.* **2020**, *32*, 2003479.

(43)   Nakajima, S. The crystal structure of $Bi_2Te_{3-x}Se_x$. *J. Phys. Chem. Solids* **1963**, *24*, 479-485.

(44)   Cheng, L.; Liu, H. J.; Zhang, J.; Wei, J.; Liang, J. H.; Shi, J.; Tang, X. F. Effects of van der Waals interactions and quasiparticle corrections on the electronic and transport properties of Bi_2Te_3. *Phys. Rev. B* **2014**, *90*, 085118.

(45)   Luo, X.; Sullivan, M. B.; Quek, S. Y. First-principles investigations of the atomic, electronic, and thermoelectric properties of equilibrium and strained Bi_2Se_3 and Bi_2Te_3 including van der Waals interactions. *Phys. Rev. B* **2012**, *86*, 184111.

(46)   Gerra, G.; Tagantsev, A. K.; Setter, N.; Parlinski, K. Ionic polarizability of conductive metal oxides and critical thickness for ferroelectricity in $BaTiO_3$. *Phys. Rev. Lett.* **2006**, *96*, 107603.

(47)   Wortmann, D. The FLEUR code. https://www.flapw.de, doi: 10.5281/zenodo.7891361.

(48)   Cao, J.-J.; Gou, X.-F. First-principles study of electronic structure, phonons and electron-phonon interaction in hexagonal PdTe. *Phys. C: Supercond. Appl.* **2016**, *520*, 19-23.

(49)   Vasdev, A.; Sirohi, A.; Hooda, M. K.; Yadav, C. S.; Sheet, G. Enhanced, homogeneously type-II superconductivity in Cu-intercalated $PdTe_2$. *J. Phys. Condens. Matter.* **2020**, *32*, 125701.

(50)   Salis, M. V.; Rodiere, P.; Leng, H.; Huang, Y. K.; de Visser, A. Penetration depth study of the type-I superconductor $PdTe_2$. *J. Phys. Condens. Matter.* **2018**, *30*, 505602.

(51)   Sirohi, A.; Das, S.; Adhikary, P.; Chowdhury, R. R.; Vashist, A.; Singh, Y.; Gayen, S.; Das, T.; Sheet, G. Mixed type I and type II superconductivity due to intrinsic electronic inhomogeneities in the type II Dirac semimetal $PdTe_2$. *J. Phys. Condens. Matter.* **2019**, *31*, 085701.

(52)   Liu, W.; Li, S.; Wu, H.; Dhale, N.; Koirala, P.; Lv, B. Enhanced superconductivity in the Se-substituted 1T-$PdTe_2$. *Phys. Rev. Mater.* **2021**, *5*, 014802.

(53)   Zhang, H.; Liu, C.-X.; Qi, X.-L.; Dai, X.; Fang, Z.; Zhang, S.-C. Topological insulators in Bi_2Se_3, Bi_2Te_3 and Sb_2Te_3 with a single Dirac cone on the surface. *Nat. Phys.* **2009**, *5*, 438-442.

(54)   Rüßmann, P.; Blügel, S. Proximity induced superconductivity in a topological insulator. *doi:10.48550/arXiv.2208.14289.*

(55)   Shen, J.; He, W.-Y.; Yuan, N. F. Q.; Huang, Z.; Cho, C.-w.; Lee, S. H.; Hor, Y. S.; Law, K. T.; Lortz, R. Nematic topological superconducting phase in Nb-doped Bi_2Se_3. *Npj Quantum Mater.* **2017**, *2*, 59.

(56)   Wang, J.; Ran, K.; Li, S.; Ma, Z.; Bao, S.; Cai, Z.; Zhang, Y.; Nakajima, K.; Ohira-Kawamura, S.; Cermak, P.; Schneidewind, A.; Savrasov, S. Y.; Wan, X.; Wen, J. Evidence for singular-phonon-induced nematic superconductivity in a topological superconductor candidate $Sr_{0.1}Bi_2Se_3$. *Nat. Commun.* **2019**, *10*, 2802.

(57)   Wang, J.; Zhang, S. C. Topological states of condensed matter. *Nat. Mater.* **2017**, *16*, 1062-1067.

(58)   Barthel, J. Dr. Probe: A software for high-resolution STEM image simulation. *Ultramicroscopy* **2018**, *193*, 1-11.

(59)   Ebert, H.; Ködderitzsch, D.; Minár, J. Calculating condensed matter properties using the KKR-Green's function method-recent developments and applications. *Rep. Prog. Phys.* **2011**, *74*, 096501.

(60)   The JuKKR code, https://jukkr.fz-juelich.de, doi: 10.5281/zenodo.7284739.

(61)   Rüßmann, P.; Blügel, S. Density functional Bogoliubov-de Gennes analysis of superconducting Nb and Nb(110) surfaces. *Phys. Rev. B* **2022**, *105*, 125143.

(62)   Rüßmann, P.; et al. JuDFTteam/aiida-kkr: AiiDA-KKR (v1.1.11-dev). Zenodo doi:10.5281/zenodo.3663525.

(63)   Rüßmann, P., Bertoldo, F. & Blügel, S. The AiiDA-KKR plugin and its application to high-throughput impurity embedding into a topological insulator. *Npj Comput. Mater.* **2021**, *7*, 13.

(64)   Bröder, J.; et al. JuDFTteam/aiida-fleur: AiiDA-FLEUR (v.1.3.1). Zenodo doi:10.5281/zenodo.6420726.

(65)   Bröder, J.; Wortmann, D.; & Blügel, S. Using the AiiDA-FLEUR package for all-electron ab initio electronic structure data generation and processing in materials science. In *Extreme Data Workshop 2018 Proceedings*, **2019**, vol *40*, p43-48.

(66)   Huber, S. P.; Zoupanos, S.; Uhrin, M.; Talirz, L.; Kahle, L.; Hauselmann, R.; Gresch, D.; Muller, T.; Yakutovich, A. V.; Andersen, C. W.; et al. AiiDA 1.0, a scalable computational infrastructure for automated reproducible workflows and data provenance. *Sci. Data* **2020**, *7*, 300.

(67)   Wilkinson, M. D.; Dumontier, M.; Aalbersberg, I. J.; Appleton, G.; Axton, M.; Baak, A.; Blomberg, N.; Boiten, J. W.; da Silva Santos, L. B.; Bourne, P. E.; et al. The FAIR guiding principles for scientific data management and stewardship. *Sci. Data* **2016**, *3*, 160018.

(68)   Talirz, L.; Kumbhar, S.; Passaro, E.; Yakutovich, A. V.; Granata, V.; Gargiulo, F.; Borelli, M.; Uhrin, M.; Huber, S. P.; Zoupanos, S.; et al. Materials Cloud, a platform for open computational science. *Sci. Data* **2020**, *7*, 299.

(69)   Rusu, D.; Peters, J. J. P.; Hase, T. P. A.; Gott, J. A.; Nisbet, G. A. A.; Strempfer, J.; Haskel, D.; Seddon, S. D.; Beanland, R.; Sanchez, A. M.; et al. *Materials Cloud Archive*, doi:10.24435/materialscloud:ky-mp.
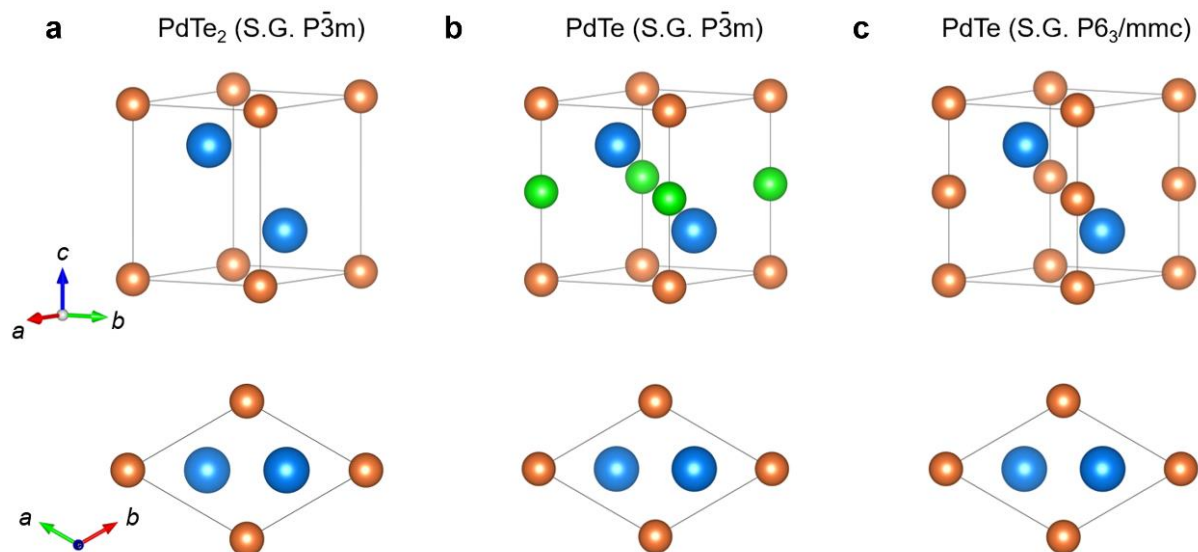
SUPPLEMENTARY MATERIAL

Figure S1. Comparison between different structural phases. a-c) Crystal structures of $PdTe_2$ and PdTe with space group (S.G.) $P\bar{3}m$, and PdTe with S.G. $P6_3/mmc$, respectively. The atom types are colored in blue (Te), orange (Pd) and green (intercalated Pd). The top row is the stereo view and the bottom row is the projection view along the c axis.
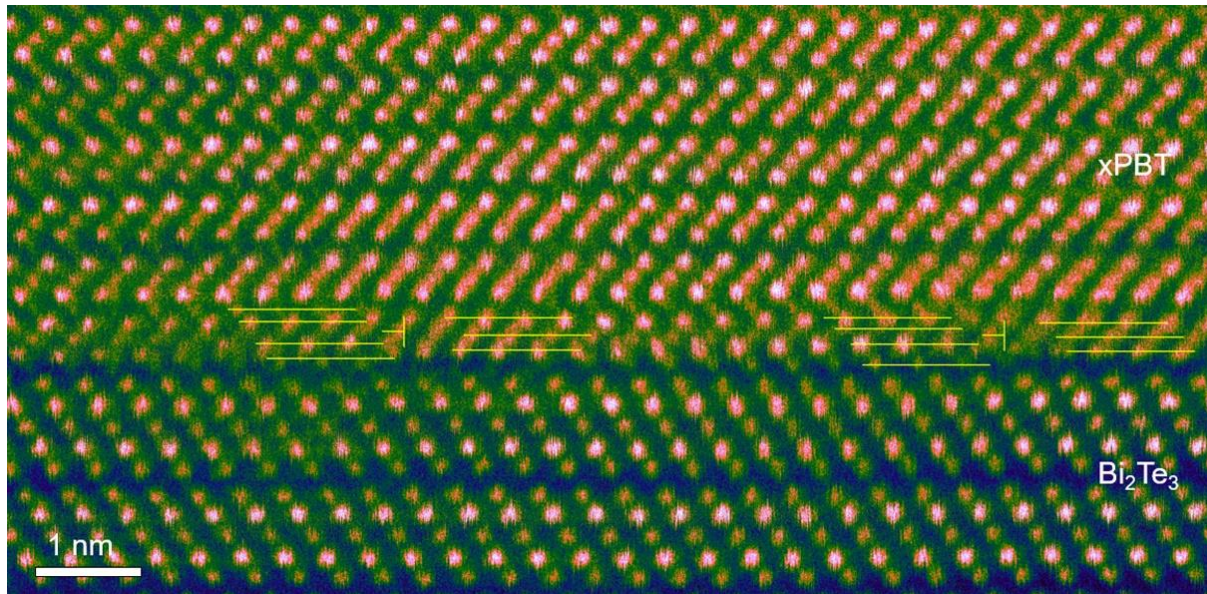
Figure S2. Atomic-resolution xPBT/Bi₂Te₃ interface. Yellow solid lines are marked on the HAADF image to show an additional component of the interfacial mismatch dislocation caused by asymmetric Pd accumulation.

a

Legend: 🟠 Pd   🔵 Bi/Te   🟢 Intercalated Pd
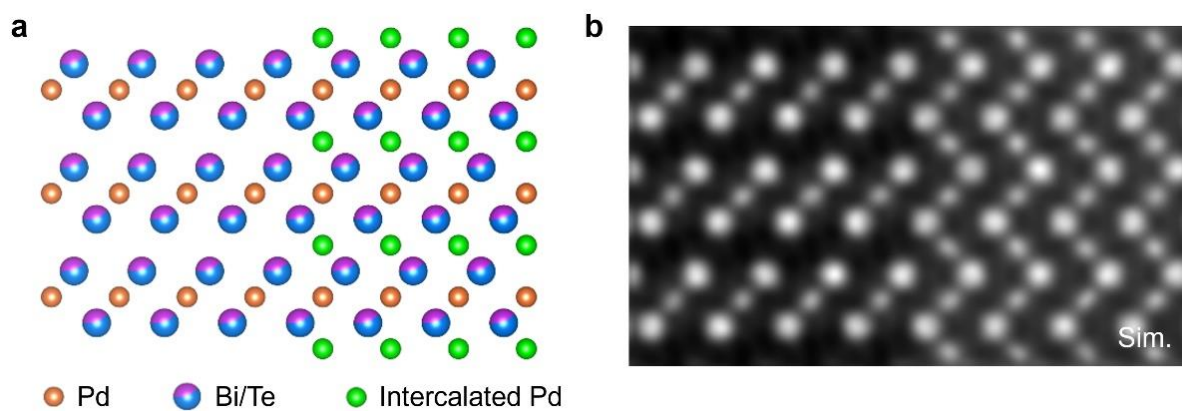
b Sim.

Figure S3. Image simulation on the xPBT phase. a) Structural model with and without Pd intercalation. **b**) Simulated HAADF image with a thickness of 43.2 nm.
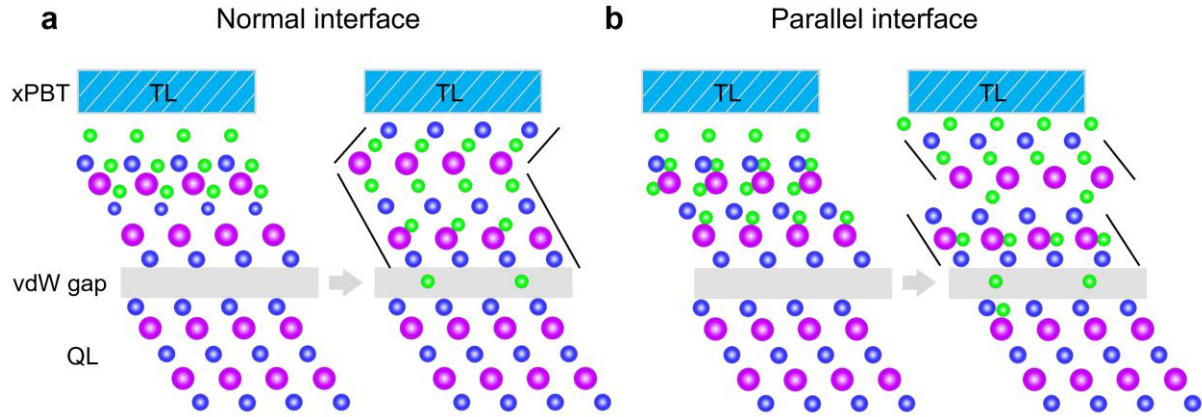
Figure S4. Schematic Pd diffusion pathways. a,b) Possible formation of normal-mode and parallel-mode contact interfaces, respectively. Although the breaking of Bi-Te bonds by intercalated Pd atoms dominates in both scenarios, it seems that the intercalation at the vdW gaps may suppress the chemical diffusion, as manifested by the highly condensed ε_{yy} strain.
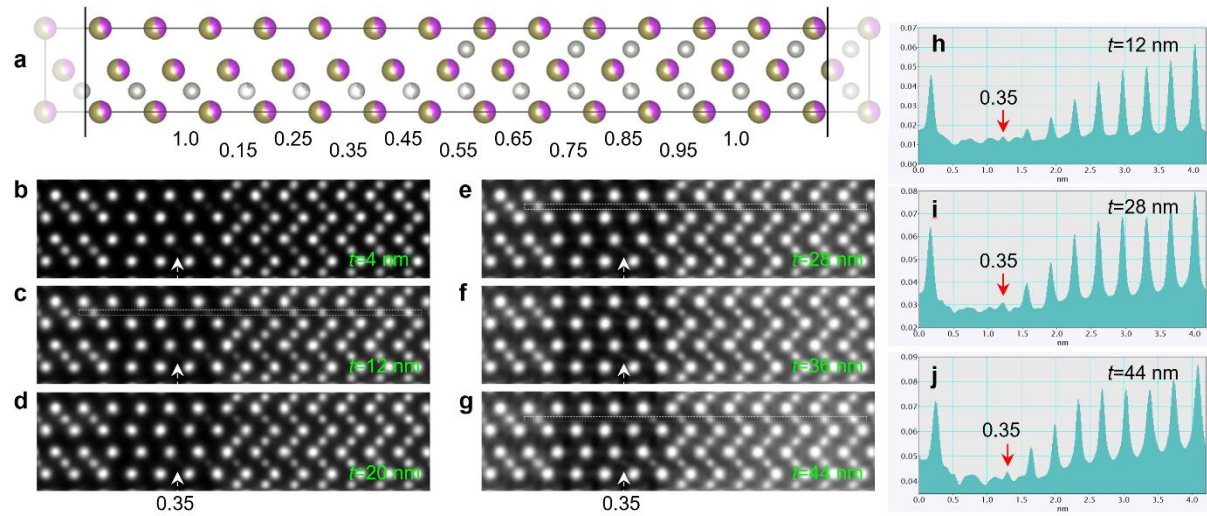
Figure S5. HAADF image simulation of Pd intercalation with different occupancy at the vdW gaps. a) Structure model. **b-g)** Simulated HAADF images with thickness ranging from 4 to 44 nm. **h-j)** Intensity profiles extracted from images of c), e) and g), respectively.
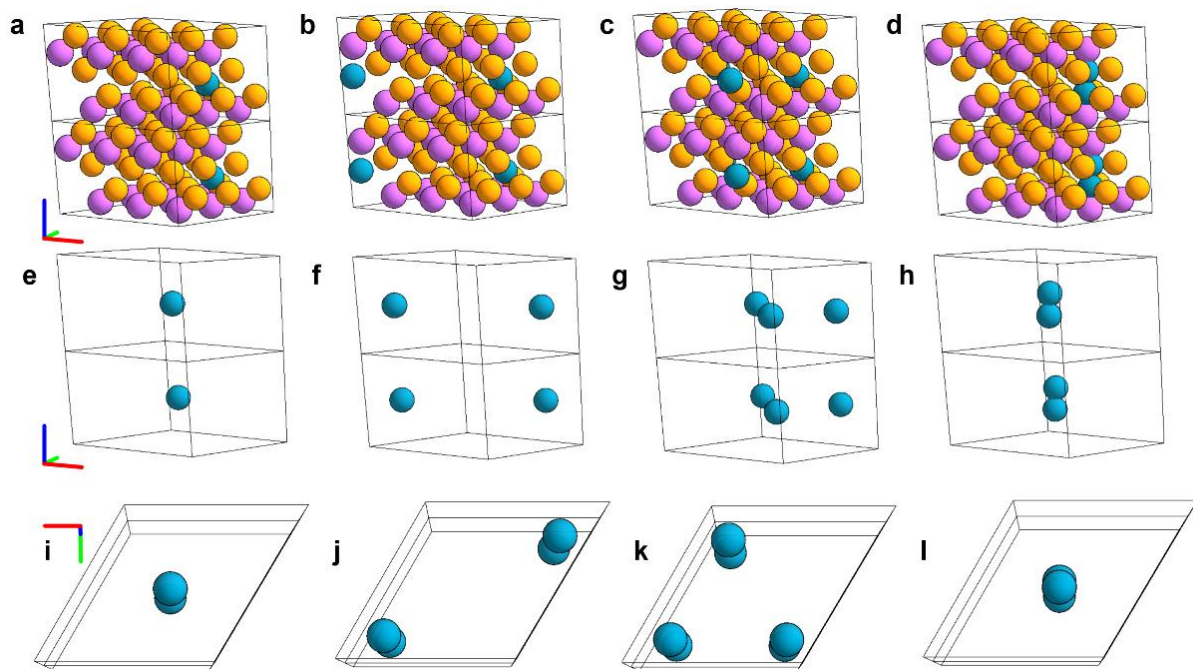
Figure S6. Relaxed position of Pd atoms intercalated in the vdW gap of Bi₂Te₃. a-d) Relaxed positions of one to three Pd atoms in a $3 \times 3 \times 1$ Bi$_2$Te$_3$ supercell, calculated with the FLEUR code. The atom types are Pd (blue), Bi (pink) and Te (orange). **e-h**) Side view of only the Pd atoms, respectively. **i-l**) Top view of the Pd atoms in the unit cells, respectively. When the Pd concentration is low, a-c), the individual Pd atoms remain in the center of the vdW gap. Only when two Pd atoms occupy the same hollow site d), the Pd atoms repel each other and are pushed deeper into the QL, ending up at roughly the same height as the neighboring Te atoms.
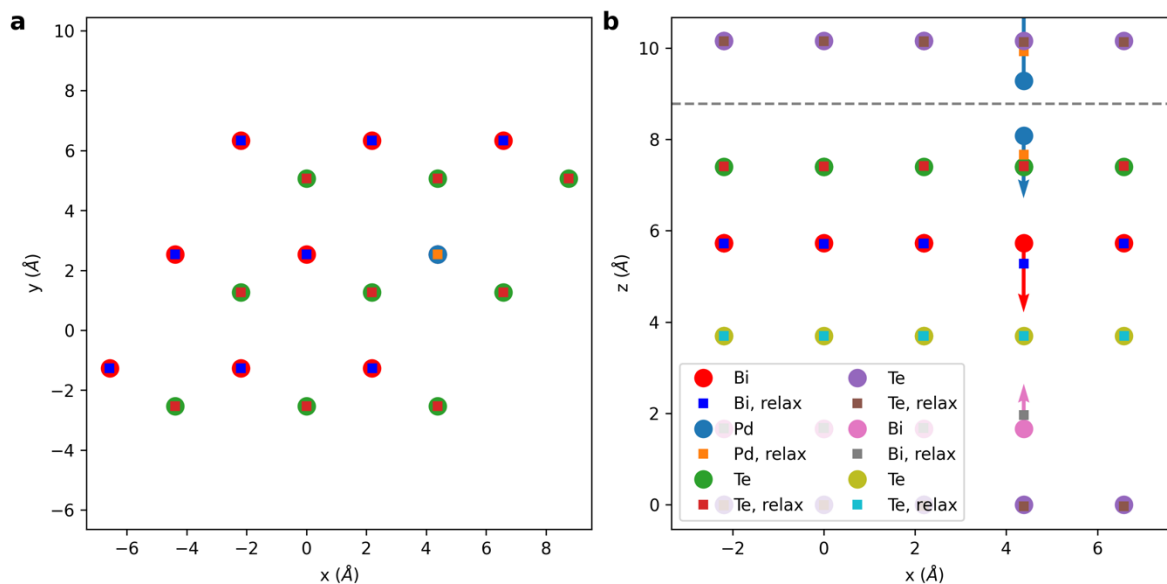
Figure S7. Broken symmetry upon Pd interaction in Bi₂Te₃. a) [001] view of the Pd-intercalated Bi₂Te₃. **b)** [1$\bar{1}$0] view showing the relaxation of Bi₂Te₃ with two Pd atoms intercalated at the vdW (grey dashed line) gap as illustrated in Fig. S6d. The original and relaxed positions are indicated by colored spheres and squares, respectively. The direction of the atom relaxation is highlighted by color arrows. One can see that the atoms relax only considerably along *z*-direction of Bi₂Te₃. With inward movement of Pd atoms into the outermost Te layer of the Bi₂Te₃ quintuple layer (QL), the underlying Bi atoms (red circle with arrow and relaxed blue square) are attracted towards the center of the QL.
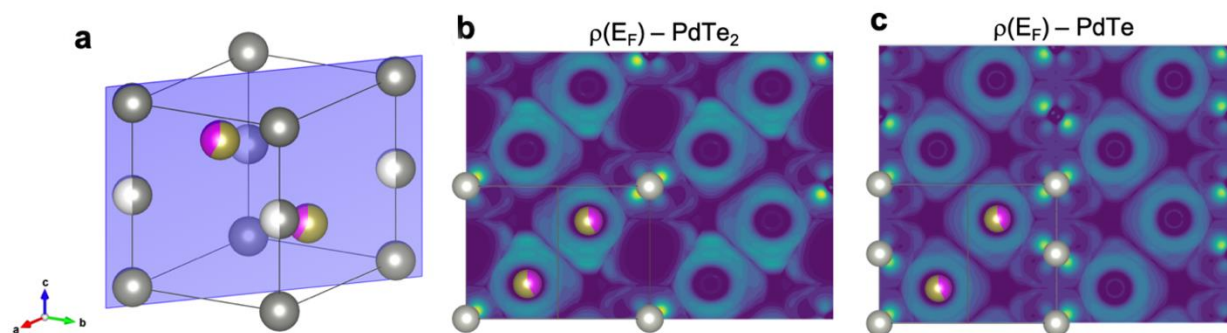
Figure S8. Electron density distribution in PdTe and PdTe₂. a) Unit cell of PdTe$_x$ where the blue shaded surface highlights the plane in which the charge density at the Fermi level is visualized for **b)** PdTe$_2$ and **c)** PdTe. The additional Pd atoms in c) add additional states (zig-zag pattern in vertical direction along the line formed by Pd atoms) that leads to an increased metallicity and enhanced superconductivity in PdTe compared to PdTe$_2$.
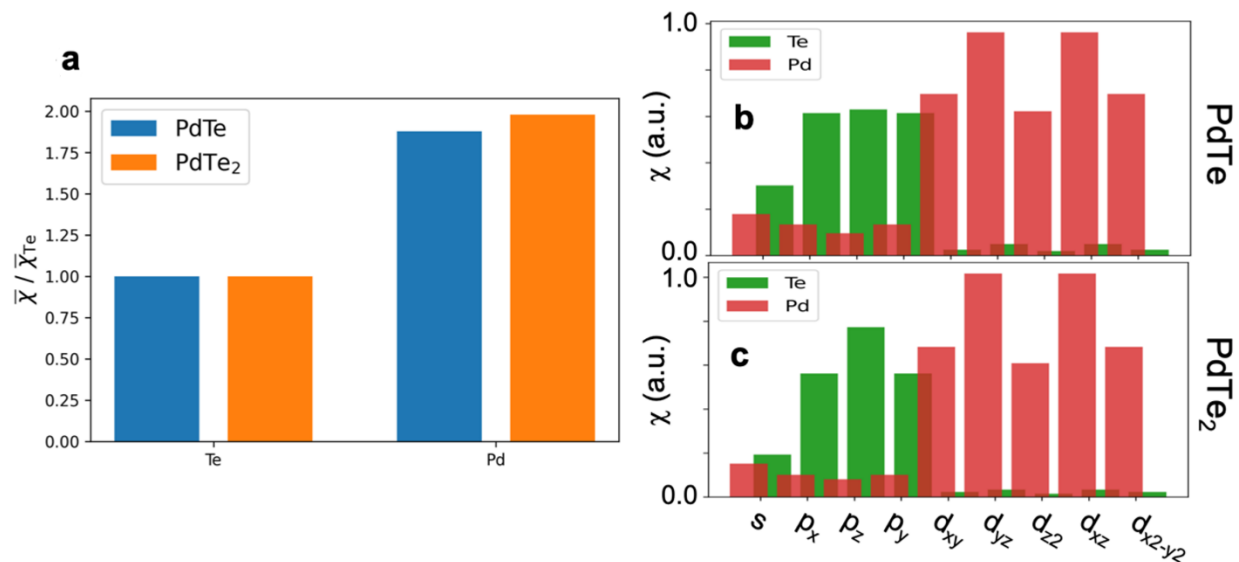
Figure S9. Atom and orbital resolved anomalous density of PdTe and PdTe₂. a) Atom resolved anomalous density for PdTe (blue) and PdTe₂ (orange) relative to the contribution of one Te atom. **b,c**) Atom and orbital resolved anomalous density for PdTe (b) and PdTe2 (c).
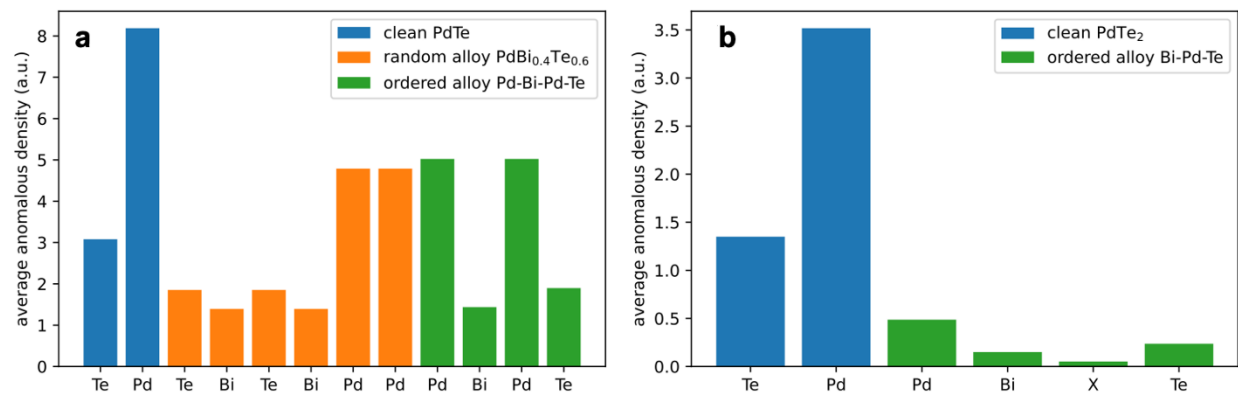
Figure S10. Atom resolved anomalous density in different xPBT phases. a) Atom-resolved anomalous density in clean PdTe (blue), the random alloy $PdBi_{0.4}Te_{0.6}$ and in the ordered alloy Pd_2BiTe. **b)** Atom resolved anomalous density in clean $PdTe_2$ and the ordered alloy phase of PdBiTe.
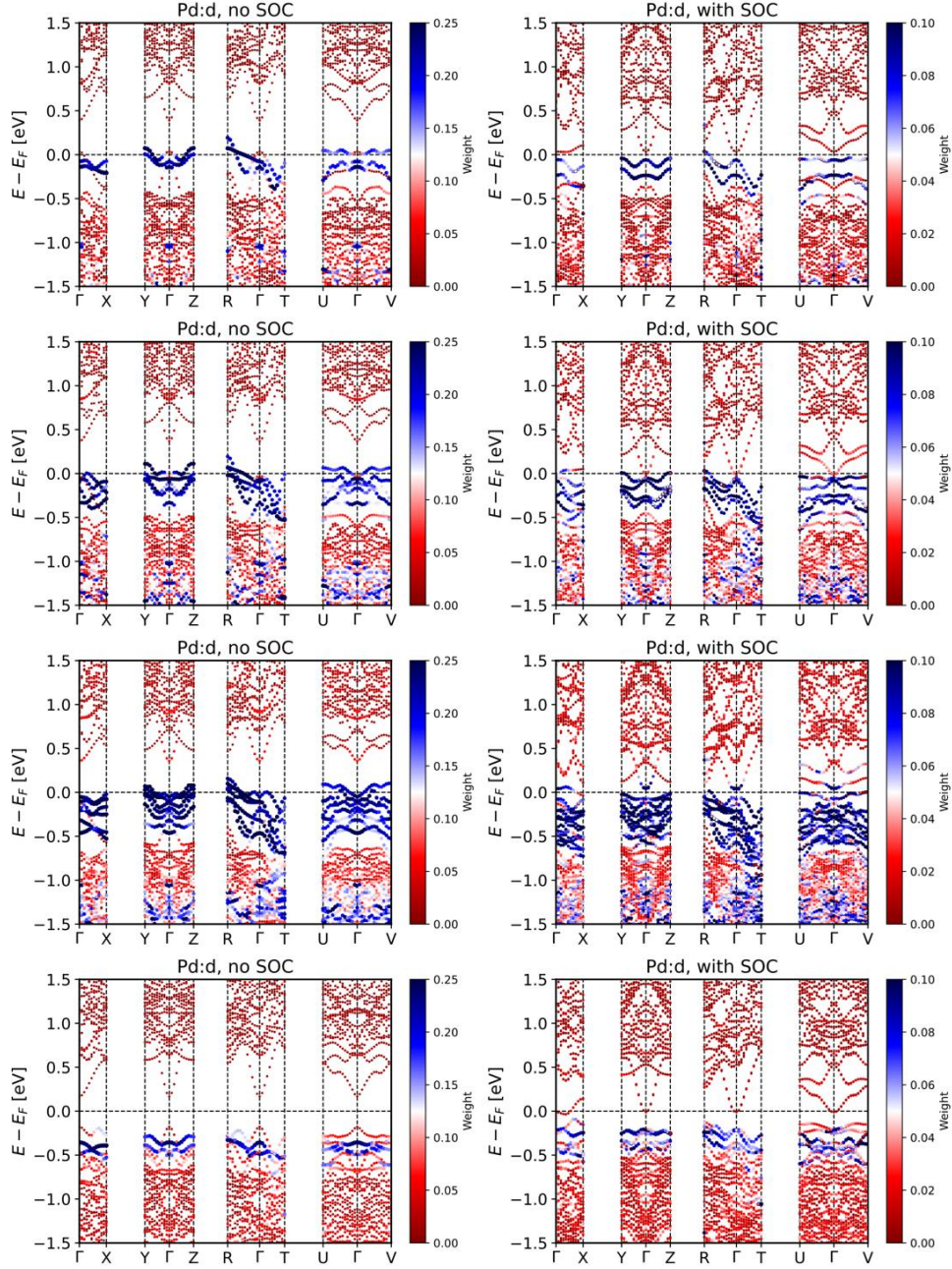
Figure S11. Contribution of Pd *d* orbitals to the band structure of Pd-intercalated Bi₂Te₃. The four rows correspond (from top to bottom) to the structural models given in Fig. S6 (a-d) for one to three Pd atoms intercalated into the vdW gap of a $3 \times 3 \times 1$ Bi₂Te₃ supercell. The last row corresponds to the experimentally observed position of Pd atoms at larger concentration. The Pd *d*-states are highlighted in blue. Left column: band structure without SOC, right column: band structure including SOC.
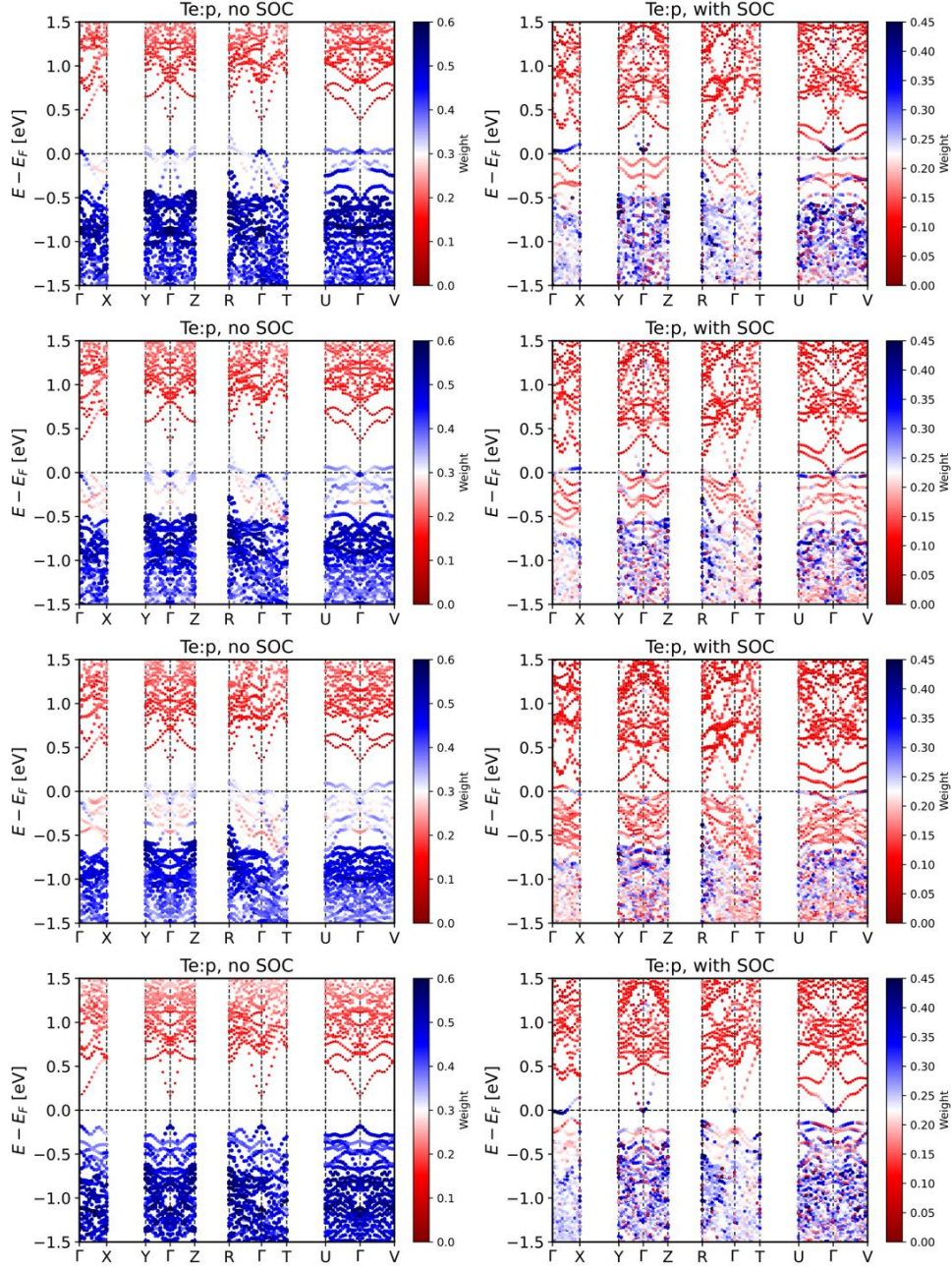
Figure S12. Contribution of Te *p* orbitals to the band structure of Pd-intercalated Bi₂Te₃.
Layout of the plots as in Figure S8 but the blue colors highlight the Te *p*-states for the four structural model given in Fig. S6(a-d). Without SOC (left column) the valence band is made up of predominantly Te *p*-states whereas the conduction band (CB) is of predominantly Bi *p* character. With SOC (right column) the topological band inversion is visible around Γ as the blue color at the bottom of the CB. This is only weakened in the third row where many Pd *d*-states are present inside the Bi₂Te₃ in the band gap (cf. Fig. S10).

Table S1. Experimental superconducting transition temperatures T_C of different $PdTe_x$ compounds.

Material	T_C [K]	References
PdTe	4.5	Refs. 30, 31
$PdTe_2$	~1.7	Refs. 28, 29, 50, 51
$Pd(Te,Se)_2$	2.74	Ref. 52
Cu-intercalated $PdTe_2$	2.4	Ref. 49
$Pd-Bi_2Te_3$	0.67-1.22	Ref. 33